ACS NANO

www.acsnano.org

ARTICLE

Hybrid Nanocrystals of Small Molecules and Chemically Disordered Polymers

Eric P. Bruckner,[#] Tine Curk,[#] Luka Đorđević, Ziwei Wang, Yang Yang, Ruomeng Qiu, Adam J. Dannenhoffer, Hiroaki Sai, Jacob Kupferberg, Liam C. Palmer, Erik Luijten,* and Samuel I. Stupp*

Cite This: *ACS Nano* 2022, 16, 8993−9003

Read Online

ACCESS | Metrics & More | Article Recommendations | Supporting Information

ABSTRACT: **Organic crystals formed by small molecules can be highly functional but are often brittle or insoluble structures with limited possibilities for use or processing from a liquid phase. A possible solution is the nanoscale integration of polymers into organic crystals without sacrificing long-range order and therefore function. This enables the organic crystals to benefit from the advantageous mechanical and chemical properties of the polymeric component. We report here on a strategy in which small molecules cocrystallize with side chains of chemically disordered polymers to create hybrid nanostructures containing a highly ordered lattice. Synchrotron X-ray scattering, absorption spectroscopy, and coarse-grained molecular dynamics simulations reveal that the polymer backbones form an "exo-crystalline" layer of disordered chains that wrap around the nanostructures, becoming a handle for interesting properties. The morphology of this "hybrid bonding polymer" nanostructure is dictated by the competition between the polymers' entropy and the enthalpy of the lattice allowing for control over the aspect ratio of the nanocrystal by changing the degree of polymer integration. We observed that nanostructures with an exo-crystalline layer of polymer exhibit enhanced fracture strength, self-healing capacity, and dispersion in water, which benefits their use as light-harvesting assemblies in photocatalysis. Guided by computation, future work could further explore these hybrid nanostructures as components for functional materials.**

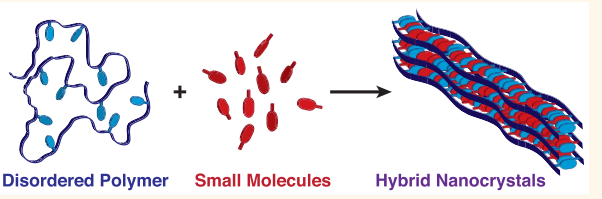

KEYWORDS: *hybrid bonding polymers, supramolecular polymers, polymer crystallization, nanoribbons, coarse-grained simulations, polymer fracture mechanics, polymer photocatalysis*

The precise spatial arrangement of organic molecules into well-defined periodic lattices at the nanoscale would be of great interest to the design of functional soft nanostructures and materials. Such structures could have attractive functions in photocatalysis,[1] photovoltaics,[2] ferroelectrics,[3,4] proton exchange membranes,[5] and quantum information systems,[6] where crystallinity can have a dramatic effect on charge and ion transport along with qubit−qubit coupling. Living systems build ordered structures with sequence-defined polymers, such as polypeptides and polynucleotides, that are highly functional without relying on the formation of single crystals. For example, polypeptides form functional structures by positioning organic residues at precise locations at the nanoscale through the folding of polymer chains into identical objects. In the cell nucleus, polynucleotides engage in precise base pairing and regular nanoscale conformation of the double helix, but these structures are aperiodic at larger length scales. This level of spatial precision remains a difficult task in synthetic soft material systems due to kinetic barriers present during the crystallization of polymer chains and the complicated synthesis of sequence-defined and stereoregular macromolecules. Thus, a major challenge remaining in the design of functional soft materials is the development of methods to control the crystalline packing and arrangement of synthetic macromolecules at the nanoscale.

In recent promising work, the degree of crystallinity and the crystal structure of ion-containing polymers were controlled through the sequence defined synthesis of carboxylic[7−10] and sulfonic acid[11,12] bearing polyolefins, which allowed for the design of crystalline polymers with high proton conductivity.[5] Similar findings have also been shown in systems containing monodisperse telechelic polyethylenes,[13,14] which form layered aggregates of crystalline polymers with layer spacings that are dependent on chain length. Crystallization-driven self-assembly

Received: January 9, 2022
Accepted: May 16, 2022
Published: May 19, 2022

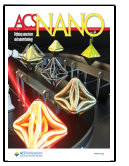

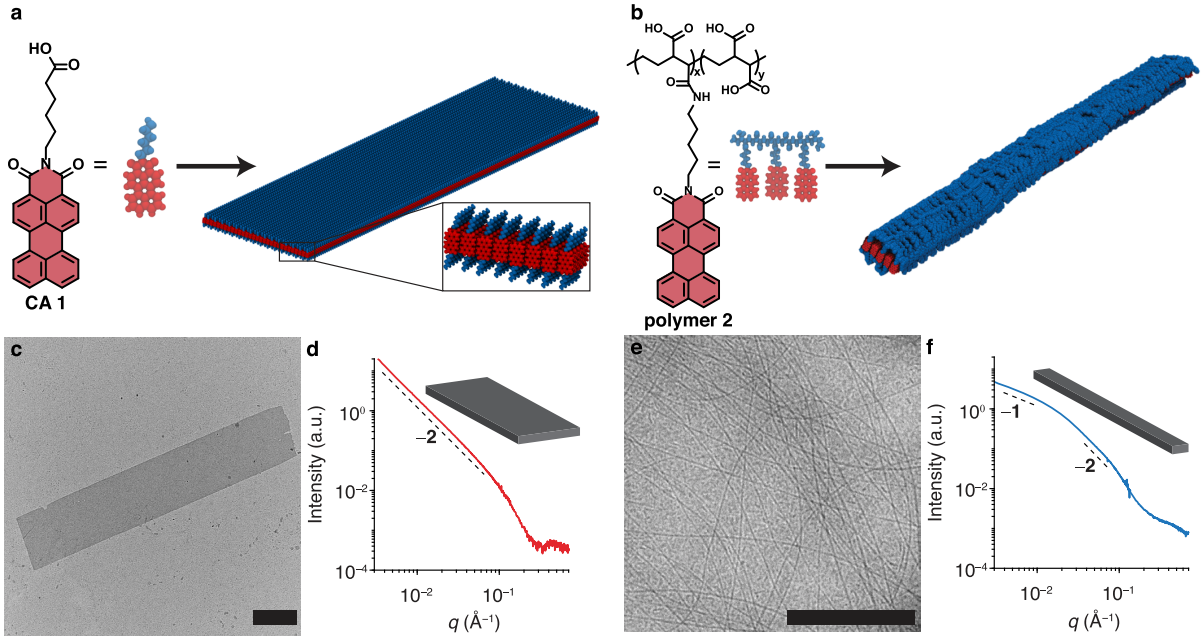

Figure 1. Self-assembly of the supramolecular and covalent polymers. (a) Chemical structure of the PMI CA (CA 1) and schematic representation of the self-assembled supramolecular polymer. (b) Chemical structure of the PMI-functionalized random copolymer (polymer 2) and schematic representation of the structure formed based on a combination of the cryogenic transmission electron microscopy (cryo-TEM), SAXS, WAXS, and computer simulation data. (c) TEM micrographs of CA 1 stained with a 1 wt % solution of uranyl acetate revealing formation of large, ribbon-like structures. (d) SAXS patterns of CA 1 showing slope −2 in the Guinier region indicative of a wide ribbon morphology. (e) Cryo-TEM micrographs of polymer 2 at 30% functionalization showing formation of a fibrous, thin ribbon architecture. (f) SAXS patterns of polymer 2 at 30% functionalization showing a transition from slope −1 to slope −2 in scattering intensity as a function of scattering vector q, defined as $q = 4\pi \sin\theta/\lambda$, where θ is half of the total scattering angle and λ is the X-ray wavelength. Scale bars = 500 nm.

is another emerging technique to precisely control the nanoscale morphology of crystallizable block copolymers by enabling the formation of multicomponent, core−shell nanostructures.[15−17] This technique has led to the recent development of crystalline nanofibers for applications in long-range exciton transport[18] and photocatalytic hydrogen production[19] with poly(di-*n*-hexylfluorene)- and poly(ferrocene-dimethylsilane)-based block copolymers, respectively. Changes in the crystallinity and morphology of self-assembling block copolymers can be controlled through the addition of surfactants, such as cetyltrimethylammonium bromide[20] and bis(2-ethylhexyl) sulfosuccinate sodium salt,[21] which change the degree of phase separation between the two polymer blocks.

Advanced processing techniques have also been employed to direct the crystallization and local ordering of soft materials. High-strength external magnetic fields were shown to direct the self-assembly of columnar mesophases of discotic liquid crystals into aligned, crystalline domains.[22−24] Electric[25] and magnetic[26] fields have been used to align liquid crystal elastomers into single-crystal orientations, and photopatterning techniques[27,28] have been shown to control the surface alignment of liquid crystal domains to enable soft actuating materials. Thermal processing and sintering is another method used to control the grain size in macroscopic objects of nanoparticle superlattices composed of inorganic nanoparticle cores coated with a polymer brushes.[29] Despite these advances in controlling the crystalline ordering of soft materials, the methods used require complicated synthetic pathways or processing equipment, which can limit their applicability to other systems.

Since synthetic polymers are at best semicrystalline materials, many other functionally interesting and stable structures may be discovered in systems where at least specific parts of a polymer can be positioned in a crystalline lattice. For example, plants position light-harvesting dye aggregates and catalytic enzymes in precise positions within liquid crystalline lipid membranes in order to achieve photosynthesis.[30,31] Inspired by such noncanonical ordered systems, we considered that it would be interesting to integrate readily accessible covalent polymers, lacking both sequence specificity and stereoregularity, with crystallizable organic molecules to create robust hybrid nanostructures that contain ordered lattices. While covalent polymers have been integrated with self-assembling organic molecules to improve mechanical properties,[32−34] induce nanostructural changes,[35,36] and provide a favorable crystallization environment,[37−39] these approaches have been unable to access structures in which the covalent polymers and small molecules have cocrystallized into the same lattice.

RESULTS AND DISCUSSION

Hybrid Nanocrystal Formation and Nanostructure Morphology. We report here on crystalline nanostructures that formed upon mixing solutions of a nonstereoregular random copolymer and a small molecule, chromophore amphiphile (CA) monomer (Figure 1a) known to form a crystalline supramolecular polymer due to a combination of $\pi-\pi$ stacking and dipolar interactions.[1] The covalent polymer (Figure 1b) and the monomers of the supramolecular polymer contained the same chemical moiety that was incorporated in the crystalline lattice, a strong visible-light absorbing

https://doi.org/10.1021/acsnano.2c00266
ACS Nano 2022, 16, 8993−9003

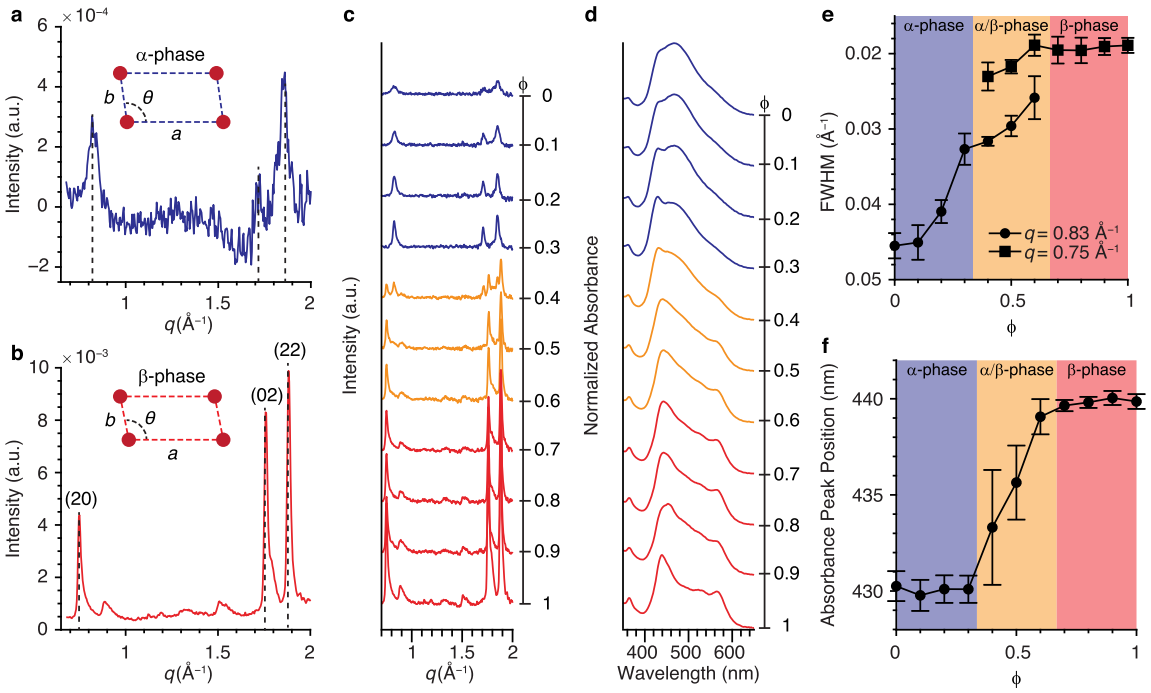

Figure 2. Cocrystallization of CA 1 and polymer 2 to form a hybrid bonding polymer. (a) WAXS patterns of polymer 2 at 30% functionalization showing the formation of an α-phase with a suggested 2D oblique lattice with intermolecular spacings of a = 7.6 Å, b = 3.7 Å, and θ = 94.0°. (b) WAXS patterns of CA 1 showing the formation of a β-phase with a 2D oblique lattice with intermolecular spacings of a = 8.3 Å, b = 3.6 Å, and θ = 92.5°. (c, d) WAXS patterns (c) and UV−vis absorption spectra (d) for coassemblies of polymer 2 at 30% functionalization and CA 1 at different coassembly ratios ϕ; WAXS patterns corresponding to α-phase, β-phase, and the mixed α/β two-phase regions are colored in blue, red, and yellow, respectively. (e) Full width at half-maximum (FWHM) of the q = 0.83 Å^{-1} and 0.75 Å^{-1} scattering peaks showing an increase in the crystal domain size of hybrid bonding polymers with increasing ϕ. (f) Absorption peak position associated with crystalline PMI chromophores as a function of ϕ, showing the phase transition from the α-phase to the β-phase. Error bars denote the standard deviation for averages of all samples between 1% and 30% functionalization of polymer 2.

chromophore termed perylene monoimide (PMI) (Supporting Information Figures S1−S6 and Table S1). Before mixing the PMI-functionalized covalent polymer with the CA, we investigated the structures of the individual components. To drive the components toward equilibrium, we annealed them in an aqueous electrolyte to screen repulsive electrostatic forces. Under these conditions, the supramolecular monomer CA **1** assembled into interdigitated bilayers (Figure 1a) that form micron-sized nanoribbons (Figure 1c,d) as reported previously.[40] Surprisingly, we observed that the chemically disordered covalent polymer **2** formed predominantly high-aspect-ratio nanostructures with widths 2 orders of magnitude narrower than the nanoribbons formed by CA **1**, consistent with a change in slope from −1 to −2 in the small-angle region of the X-ray scattering patterns (Figure 1e,f). Under the conditions investigated, this morphology did not change with the degree of chromophore functionalization of the covalent polymer (Supporting Information Figures S7−S16).

In addition to forming distinct nanostructure morphologies, the crystalline lattices formed by CA **1** and polymer **2** were also different. Synchrotron wide-angle X-ray scattering (WAXS) from solutions of polymer **2** (Figure 2a) revealed a set of three Bragg reflections consistent with a two-dimensional (2D) oblique lattice with intermolecular spacings corresponding to a = 7.6 Å, b = 3.7 Å, and θ = 94.0°, referred to as the α-phase, which is a similar lattice structure to other PMI-based CAs.[41] On the other hand, the lattice formed by solutions of CA **1** (Figure 2b), which we refer to as the β-phase, was a 2D oblique lattice with slightly elongated intermolecular spacings relative to those of polymer **2** (a = 8.3 Å, b = 3.6 Å, and θ = 92.5°), as reported previously.[1,40] Past reports on the β-phase crystal structure formed by CA **1** have revealed that the 2D crystal unit cell contains a molecular basis consisting of four CAs with the neighboring PMI cores arranged in an antiparallel fashion and the (02) plane repeating along the long axis of the nanostructure in the $\pi-\pi$ stacking direction of the chromophores.[40] Due to the similarities in the WAXS patterns between the α- and β-phase, we expect that the chromophores in the α-phase will have analogous packing. Interestingly, the position of the Bragg peaks of structures formed by polymer **2** appeared the same regardless of the percent functionalization with the PMI chromophore (Supporting Information Figures S7−S14).

We mixed CA **1** and polymer **2** in various proportions and investigated the spectroscopic and scattering signatures generated by these systems. We found that the crystalline domains in the system behave analogously to a conventional binary alloy, revealing three distinct regions as ϕ, the fraction of chromophores in CA **1** molecules versus the total number of chromophores in the system, were changed from 0 to 1 (Supporting Information Figures S7−S15 and Table S2). As we increased the proportion of CA **1** and thus changed ϕ from 0 to 0.3, only the α-phase crystalline domain was observed by X-ray scattering, with the diffraction peaks becoming narrower (Figure 2c). In the corresponding UV−vis absorption spectra (Figure 2d), we also saw an increase in the intensity of the resolved peak at 430 nm, characteristic of the α-phase, relative to the broad peak at 480 nm, characteristic of amorphous PMI

https://doi.org/10.1021/acsnano.2c00266
ACS Nano 2022, 16, 8993−9003

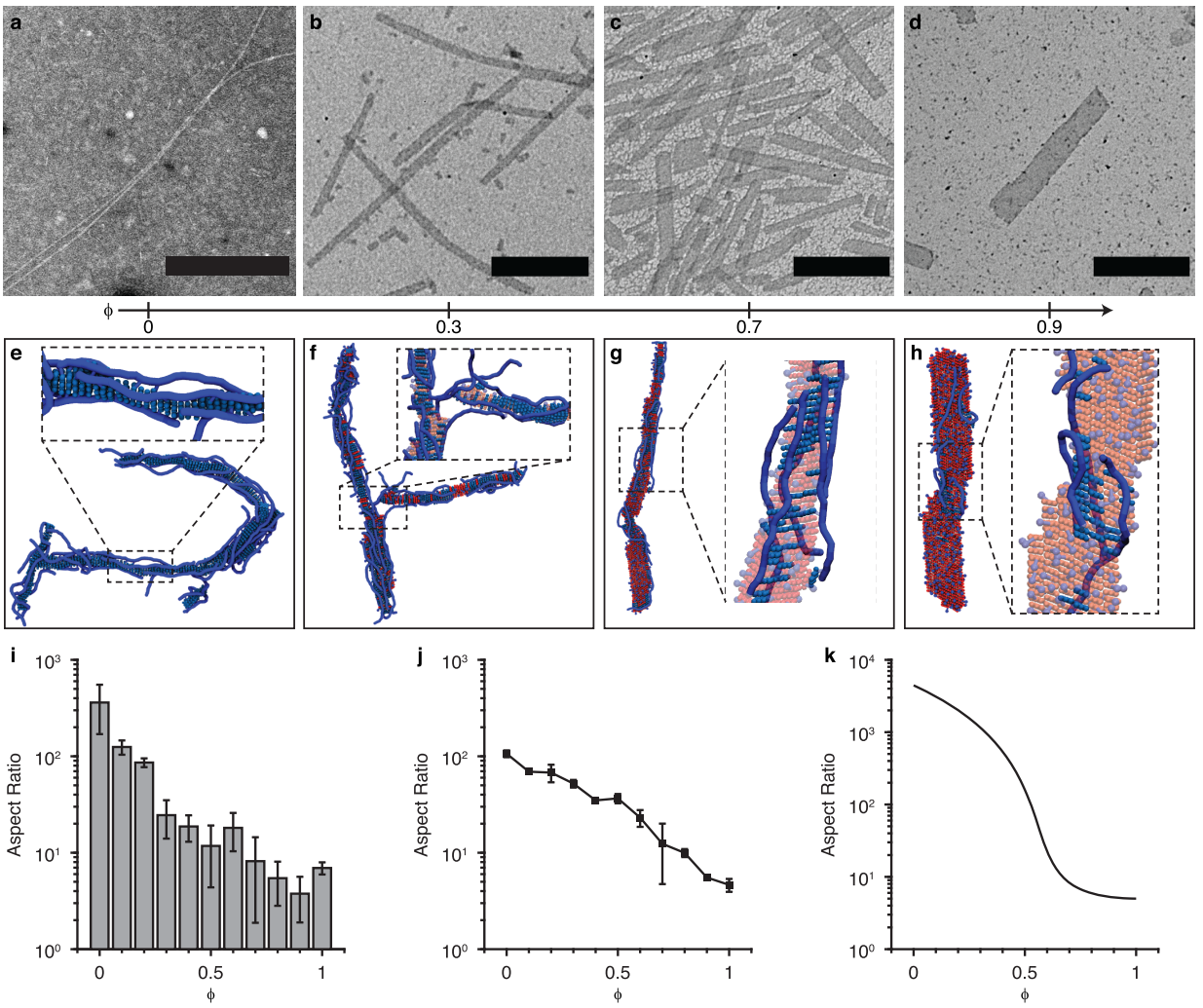

Figure 3. Changes in the nanostructure morphology of hybrid bonding polymers. (a–d) Representative conventional TEM micrographs of the HBPs containing polymer 2 at 10% functionalization and ϕ = 0 (a), ϕ = 0.3 (b), ϕ = 0.7 (c), and ϕ = 0.9 (d) stained with a 1 wt % solution of uranyl acetate, showing an increase in the width and a decrease in the aspect ratio of nanostructures formed as a function of ϕ (scale bars 500 nm). (e–h) Snapshots from the CG-MD simulations of hybrid bonding polymers at ϕ = 0 (e), ϕ = 0.3 (f), ϕ = 0.7 (g), and ϕ = 0.9 (h), showing the presence of the exo-crystalline layer; the covalent polymer backbone is colored dark blue, the covalently bonded PMI chromophores are colored light blue, and the free PMI chromophores are colored red. (i–k) Quantification of the change in aspect ratio as a function of ϕ from the TEM micrographs (i), the CG-MD simulations (j), and the theoretical prediction (k), for polymer 2 at 10% functionalization (error bars denote standard deviation).

chromophores. This indicates that CA **1** monomers were randomly incorporated with the crystalline and amorphous PMI chromophores on polymer **2**, resulting in an increase in both the α-phase fraction and the domain sizes of the crystals. As ϕ was further increased from 0.4 to 0.6, we observed a second distinct region with the appearance of X-ray scattering peaks associated with the β-phase, while those peaks characteristic of the α-phase decreased in intensity. The corresponding UV–vis absorption spectra also showed the emergence of a new peak at 580 nm, reflecting β-phase formation. Finally, for ϕ = 0.7 to ϕ = 1, the β-phase was the only phase detected in the WAXS pattern, indicating that the PMI chromophores in the covalent polymer **2** were incorporated within the β-phase formed by CA **1**. Additionally, the absorption spectra showed a resolved peak at 440 nm and the disappearance of the broad amorphous peak at 480 nm, indicating that the PMI chromophores were fully incorporated into the β-phase. Surprisingly, changing the degree of functionalization of the covalent polymer did not change the trends observed in the scattering patterns (Figure 2e) or the absorption spectra (Figure 2f), still showing a phase transition from the α-phase to the β-phase as ϕ was increased. We investigated a second system to test the generalizability of this alloying type behavior by introducing a sterically bulky substituent to the chromophore moiety (CA **3**), which has been shown to form a third crystal structure.[42,43] We obtained similar results for this system, revealing distinct regions in the phase diagram and an increase in the crystalline domain size with increasing ϕ (Supporting Information Figures S17–S25). Control experiments with CA **1** and CA **3** in the presence of unfunctionalized polymer **2** (Supporting Information Figure S26 and Table S2) further suggested that this cocrystallization phenomenon is driven by a combination of π–π stacking and dipolar interactions between PMI motifs on the covalent polymer and the small molecule CA.

The observation of crystalline structures in mixtures of a random covalent copolymer with a monomer known to form a supramolecular polymer defines the system as a hybrid

https://doi.org/10.1021/acsnano.2c00266
ACS Nano 2022, 16, 8993–9003

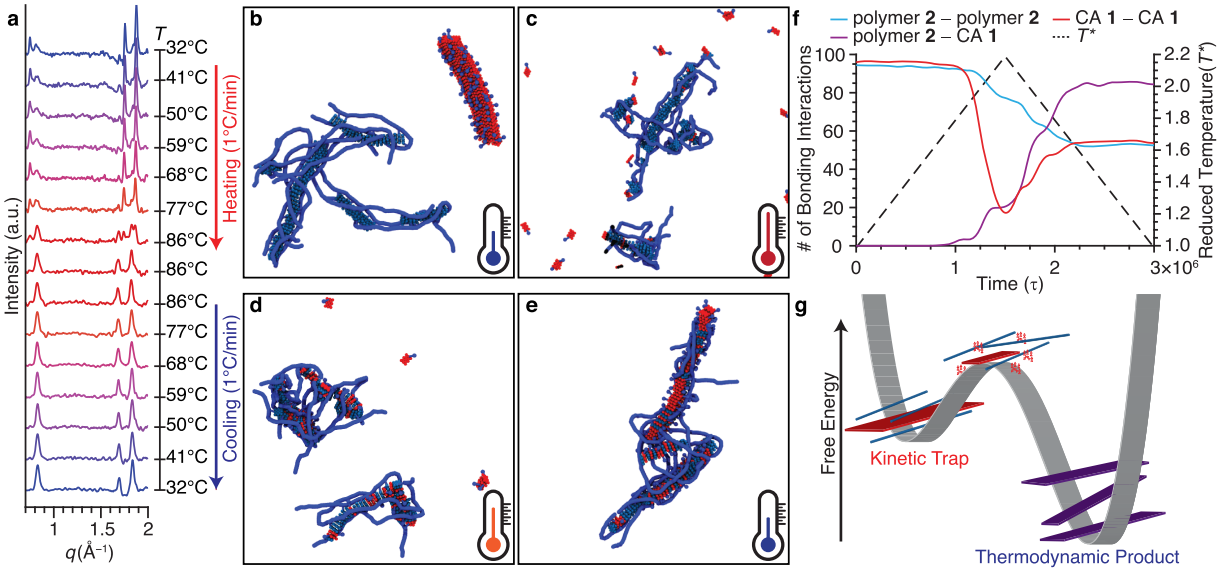

Figure 4. Determination of the free-energy landscape for the formation of hybrid bonding polymers. (a) Representative VT-WAXS patterns for the formation of ϕ = 0.3 HBPs from mixtures of polymer 2 at 30% functionalization and the supramolecular polymer CA 1 during the annealing process. (b–e) Representative snapshots of the HBPs obtained from CG-MD simulations of the annealing process (the schematic thermometers show the reduced temperature T^*). (b) Covalent and supramolecular polymers at T^* = 1.0. (c) Melting of the supramolecular polymer at T^* = 2.2. (d) Incorporation of the melted supramolecular polymer into the covalent polymer phase at T^* = 1.8. (e) Fully formed HBP nanostructures at T^* = 1.0. (f) Quantification of the annealing process via the number of bonding interactions between the different chromophores in the system. The simulation time scale $\tau \approx 10$ ns. (g) Schematic representation of the free-energy landscape for the formation of HBPs (thin blue ribbons represent the covalent polymer, wide red ribbons represent the supramolecular polymer, red clusters are the active species present during the annealing process, and purple ribbons represent the HBP).

bonding polymer (HBP).[44] In an HBP structure, the covalent and supramolecular polymers are chemically integrated by specific interactions. We characterized changes in the nanostructure morphology of the HBPs by transmission electron microscopy (TEM) and with increasing ϕ found a transition to wider nanoribbons (Figure 3a–d and Supporting Information Figures S27 and S28). The increase in width of the nanostructures was further supported by the low-q regime of small-angle X-ray scattering (SAXS) curves, which generally showed a change in slope from −1 to −2 with increasing ϕ (Supporting Information Figures S7–S13). TEM and SAXS also indicated a lack of bundled nanostructures, likely due to electrostatic repulsion between the highly charged HBP nanostructures. As the crystalline domain size increased with ϕ, we also observed the emergence of sharp edges and faceted corners on the nanostructures. To explore possible spatial arrangements of the covalent polymer and monomers of the supramolecular polymer within the HBPs and elucidate growth mechanisms, we turned to coarse-grained molecular dynamics (CG-MD) simulations.

Growth Mechanisms in Hybrid Bonding Polymers. We designed a model that is sufficiently coarse-grained to permit large-scale simulations of the aggregation, yet also accurately captures the interactions driving this process. This includes the π–π stacking, electrostatic, van der Waals, and excluded-volume interactions of the PMI chromophores as determined from the single-crystal X-ray structure,[40] the dipole, quadrupole, and octupole moments from DFT calculations, experimental values for the isodesmic binding of perylene diimides, and accurate persistence lengths of the covalent polymer backbone (Supporting Information Figure S29 and Table S3). The morphology of the structures obtained by simulated annealing matched the nanostructures observed experimentally (Figure 3e–h and Supporting Information Figure S30). Moreover, the simulations uncovered the mechanism of the ribbon-like geometry that emerged at low ϕ, revealing that the polymer backbones wrap around the nanostructures as an "exo-crystalline" layer, impeding the lateral growth of the nanocrystals. Whereas the covalent polymer backbones restricted the chromophore arrangement within the crystal lattice, surprisingly they did not significantly affect the cocrystallization of CA **1** and polymer **2**. The simulation showed that individual chromophores belonging to polymer **2** and CA **1** are randomly incorporated into the crystal lattice of the nanostructure (Figure 3g,h and Supporting Information Figure S31). To rationalize the driving forces for cocrystallization and mixing, we investigated the typical backbone conformations of the covalent polymer in the exo-crystalline layer outside the crystalline lattice. Although the polymer loses some conformational entropy upon incorporation into the structure, this is more than offset by the concomitant decrease in lattice enthalpy of the chromophores. Indeed, the radius of gyration tensor of individual polymer backbones showed that typical backbone conformations were not appreciably affected by lattice incorporation (Supporting Information Figures S32 and S33). This counterintuitive result arises from the relatively large persistence length of the polymer, which is comparable to the width of the nanostructures, yet not so large to introduce appreciable bending energy penalties.[45] This enables incorporation of the polymer into the structure, while the steric and electrostatic repulsion among backbones promotes mixing of CA **1** and polymer **2**. Thus, we infer that the cocrystallization of readily accessible covalent polymers with random sequences of structural units and supramolecular assemblies to create

https://doi.org/10.1021/acsnano.2c00266
ACS Nano 2022, 16, 8993–9003

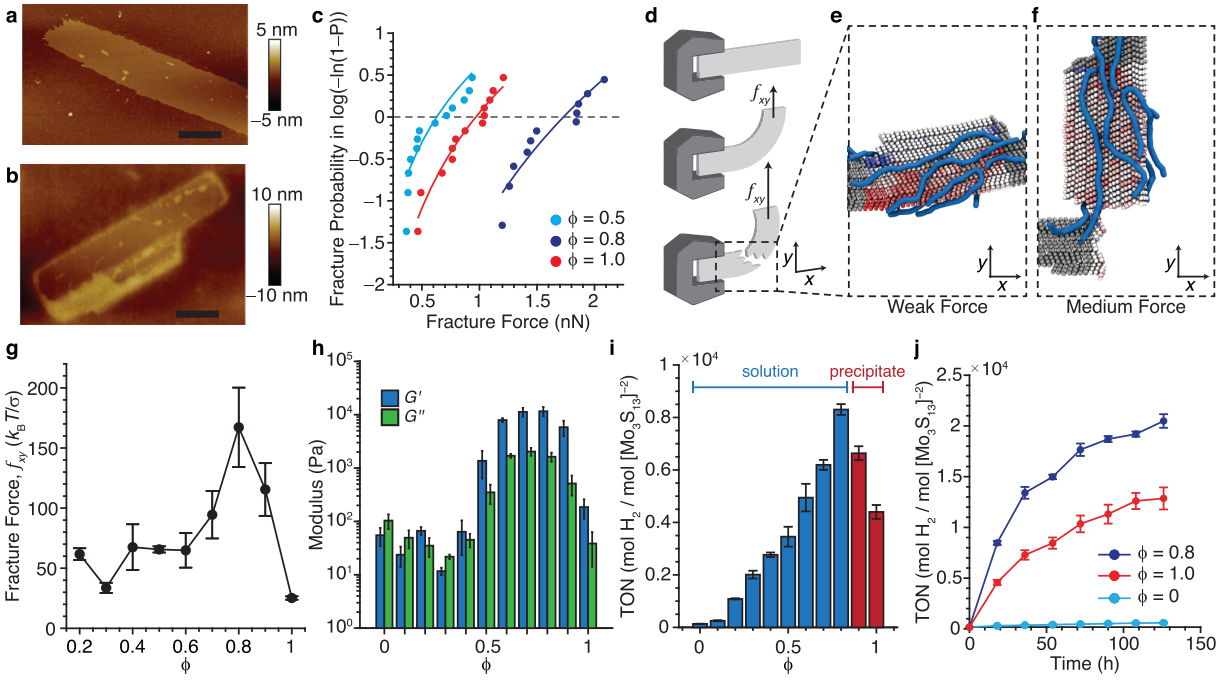

Figure 5. Improving mechanical and photocatalytic properties of organic crystals with an exo-crystalline layer of polymer. (a, b) AFM images of the supramolecular polymer (ϕ = 1.0) (a) and the hybrid bonding polymer (ϕ = 0.8) (b) (scale bars for (a) and (b) are 390 and 90 nm, respectively). (c) Probability of fracturing the structures with an AFM tip (circles), which follows a Weibull distribution (solid curves). (d) Simulation setup: The structure is clamped at the left end, and a force f_{xy} is applied to the right-hand section, leading to bending and breaking of the nanostructure. (e, f) Representative CG-MD simulation snapshots showing the fracture behavior of the HBP (ϕ = 0.8) (the clamped section of the crystal is colored in gray, whereas the nonclamped region is colored according to the local stress, from red (tensile stress) to blue (compressive stress)); the crystal lattice breaks while the covalent backbone (blue) prevents full fracture of the nanostructure. (g) Yield shear force f_{xy} to fracture a single hybrid bonding polymer nanostructure calculated using CG-MD simulations (σ is the molecular thickness of a single chromophore). (h) Storage (G') and loss (G'') moduli for cross-linked HBPs measured in the linear viscoelastic regime at an angular frequency ω = 10 s^{-1}. (i) TON of hydrogen produced with a thiomolybdate catalyst after 18 h of irradiation for HBPs formed between polymer 2 at 10% functionalization and CA 1. (j) TON values of the best performing HBP (ϕ = 0.8), the supramolecular polymer (ϕ = 1.0), and the covalent polymer (ϕ = 0) as a function of time (error bars denote standard deviation).

functional nanocrystals will require polymers having the right flexibility and repulsive backbone−backbone interactions.

These insights allow us to rationalize the morphology of the nanostructures from the balance between the free energy of confinement of the polymer as an exo-crystalline layer and the line tension of the nanostructures. Narrow structures permit the covalent polymers to wrap around the edges of the crystalline lattice and thereby minimize confinement, whereas line tension drives the formation of wider crystalline assemblies. Combining Flory−Huggins solution theory, the line tension estimated from the PMI dimerization free energy, and the experimentally observed aspect ratio at ϕ = 1 (Supporting Information equations S1−S4), we predicted the variation of the aspect ratio of the HBP structures as a function of ϕ (Figure 3k and Supporting Information Figures S34−S36). This prediction matches the observed trend and the data at high values of ϕ but overestimates the aspect ratio at low ϕ. We attribute this primarily to kinetic effects that limit the maximum size of the HBP structures, so that the equilibrium theory prediction can be regarded as an upper bound for the aspect ratio of the nanostructures in solution.

To further understand the mechanism of coassembly between the random covalent copolymers and the small molecules to form nanostructures, we obtained variable-temperature wide-angle X-ray scattering (VT-WAXS) data. We took preannealed solutions containing supramolecular polymers of CA **1** (ϕ = 1) and polymer **2** (ϕ = 0) and mixed them at room temperature at different values of ϕ. We then analyzed by WAXS these mixtures in situ as we varied the temperature (Supporting Information Figures S37 and S38). The VT-WAXS patterns (Figure 4a) showed that the initial state at room temperature contained both the α-phase of polymer **2** and the β-phase of CA **1**. As the structures were heated, the β-phase crystal of CA **1** began to melt between 68 and 77 °C and the amount of α-phase increased as indicated by a decrease in the β-phase peak intensity at q = 0.75 $Å^{-1}$ and the simultaneous growth of the α-phase peak at q = 0.83 $Å^{-1}$. After cooling to room temperature, the peaks of the α-phase persisted and the β-phase never reappeared; therefore, we conclude that CA **1** molecules were incorporated into the crystal structure of polymer **2** to create an HBP. Time-dependent absorption spectroscopy (Supporting Information Figures S39 and S40) indicated that the growth of these α-phase HBPs during the annealing process saturated around 15 min, which correlates well with the time scales previously reported for the formation of PMI-based nanostructures.[40,43]

Using our CG model, we carried out MD simulations of the annealing process to explore the mechanism of cocrystallization of CA **1** and polymer **2**. Starting from a mechanical mixture of polymer **2** nanostructures and CA **1** supramolecular polymers (Figure 4b), we observed in silico that at sufficiently high temperatures, the supramolecular polymer melted into monomers and short supramolecular oligomers of CA **1**, while the covalent polymer retained its structure (Figure 4c). These

https://doi.org/10.1021/acsnano.2c00266
ACS Nano 2022, 16, 8993−9003

monomers and oligomers acted as active species in the cocrystallization process, as they were incorporated into the crystalline lattice formed by the side groups of the covalent polymer (Figure 4d) and remained there at low temperatures (Figure 4e). We further quantified the annealing process by measuring the relative number of pairwise noncovalent interactions between the chromophores of polymer **2**, between CA **1** chromophores, and between chromophores of polymer **2** and CA **1** (Figure 4f). The results clearly showed that as the number of CA **1**−CA **1** bonding interactions decreased (melting of the supramolecular polymer), the number of polymer **2**−CA **1** interactions increased. With the combination of CG-MD and VT-WAXS experiments, we can construct an energy landscape for the formation of the HBPs (Figure 4g).

Impact of the Exo-Crystalline Layer on Material Properties. We next explored whether the hybrid nanocrystals containing the ordered lattices had mechanical properties similar to the pure crystalline supramolecular polymer. For this purpose, we probed both nanostructures using atomic force microscopy (AFM) (Figure 5a,b) and measured the relative forces required to fracture the crystals. Interestingly, using Weibull analysis for brittle materials, we found that the HBP nanostructure at ϕ = 0.8 had a significantly higher fracture strength than the supramolecular polymer (Figure 5c and Supporting Information Figures S41−46). Specifically, at a given applied stress, the probability of fracture of HBP samples was about 1 order of magnitude lower. At ϕ = 0.5, the fracture strength is comparable to that of the pure supramolecular polymer, likely as a result of the lower crystallinity (Figure 2c). Furthermore, these experiments demonstrated that HBP nanostructures healed within seconds after fracture with the AFM probe, whereas the supramolecular polymer remained in a fractured state (Supporting Information Figures S47−S50). To explain this phenomenon, we turned to CG-MD simulations (Figure 5d), which showed that the polymer in the HBP nanostructures maintained connectivity between both fragments of the crystalline lattice (Figure 5e,f). The simulations reveal that the applied stress is redistributed nonlocally due to the multiple sites at which chromophore moieties covalently linked to the polymer are inserted into the crystal. Hence, it is our interpretation that the polymer plays a key role in enhancing the probability that the fractured crystal will heal (Supporting Information Figures S47−S53). For the HBP structure, healing would not only involve the enthalpic gain when the chromophore crystal reforms but also an entropic gain since the overextended polymers adopt more favorable conformations when the two crystal pieces are closer together. Furthermore, the simulations indicate that small amounts of polymer incorporated into the nanostructure can lead to dramatic improvements in the fracture strength (Figure 5g and Supporting Information Movie S1), which was also observed with AFM experiments (Figure 5c). Conversely, incorporating large amounts of polymer leads to a narrowing of the crystalline lattices, resulting in a decrease in the fracture strength at lower values of ϕ.

This motivated us to create bulk hydrogels utilizing HBP nanostructures with different values of ϕ. The hydrogels were prepared by cross-linking the HBP nanostructures with polyethylene glycol chains. We measured both the storage and loss moduli by bulk rheology and found that HBPs at high values of ϕ both stiffened and toughened the hydrogels by approximately an order of magnitude (Figure 5h and Supporting Information Figures S54−S64) when compared to the pure, supramolecular polymer. We attribute this increase in the moduli to the high crystallinity at higher ϕ values in combination with the exo-crystalline layer of polymer that promotes gel network formation. As a result, very little random covalent polymer was necessary to obtain a significant mechanical improvement for the bulk material containing hybrid nanostructures.

Since the crystalline supramolecular polymer formed by CA **1** is known to be an effective light-harvesting assembly to photosensitize the catalytic production of hydrogen,[1,40,41,46] we explored the effect of using the hybrid nanostructures for this particular function. As previously reported,[46] the ability of PMI photosensitizers to reduce protons is highly dependent on the formation of weakly bound charge-transfer (CT) excitons, which form when PMI chromophores are in crystalline arrangements with high molecular orbital overlap. Since PMI-based HBPs exhibit changes in both their crystallinity and their crystal structure as a function of their composition, we expected to see changes in the amount of H_2 produced depending on the value of ϕ.

The catalytic performance was assessed by preparing solutions of HBP nanostructures with different values of ϕ, irradiating them in the presence of a thiomolybdate cluster (the proton reduction catalyst)[47] and ascorbic acid (the proton source and the sacrificial electron donor) and then measuring the turnover number (TON) of H_2 produced at each composition (Figure 5i). Our first important observation was that we could easily disperse the HBP nanostructures in water, whereas in earlier work, use of the pure supramolecular polymer as a light-harvesting assembly led to the formation of a hydrogel. At low values of ϕ, where the α-phase crystal structure was prevalent, the TON was very low due to the low crystallinity and inability of the α-phase crystal structure to support the formation of CT excitons.[41] When ϕ > 0.4, the β-phase crystal structure began to appear and we observed an increase in the TON. This is expected as the β-phase crystal structure has been previously shown to generate CT-excitons.[41,46] Surprisingly, the highest TONs were found for the HBP nanostructures at ϕ = 0.8, which showed a 2-fold increase in the TON of H_2 relative to TON for the supramolecular polymer formed by CA **1** (ϕ = 1). To further confirm that the HBP nanostructures outperform the pure supramolecular polymer, we followed the TONs over a period of 5 days (Supporting Information Figure S65) and observed that the hybrid system continued to be photocatalytically superior (Figure 5j). We hypothesize that the enhanced TON values originate in the high solubility of the HBP nanostructures in water as a result of the enhanced charge density contributed by the highly carboxylated polymer. In contrast, the pure supramolecular polymer of CA **1** under the conditions of the photocatalytic experiment carried out here is not fully soluble and forms a precipitate, which limits the ability of catalyst and sacrificial electron donor to come into contact (Supporting Information Figure S66). The enhancement of photocatalytic function at high values of ϕ is analogous to the mechanical robustness that emerged in hydrogels over the same range of ϕ, albeit for very different reasons. In the case of photocatalysis, very little polymer **2** content was necessary to increase the solubility of nanostructures and benefit photocatalytic activity.

https://doi.org/10.1021/acsnano.2c00266
ACS Nano 2022, 16, 8993−9003

CONCLUSIONS

The integration of covalent polymers with complementary supramolecular assemblies offers a promising strategy to create soft nanostructures and bulk materials with useful properties. By combining covalent and noncovalent association of structural units, we were able to coassemble at the nanoscale a random copolymer with small molecules to form crystalline organic lattices. These hybrid bonding polymer nanostructures exhibited functions enhanced by the insertion of the polymer into a crystalline lattice of chromophores. The polymers generated hybrid nanostructures with increased fracture strength relative to the brittle pure crystals and provided a mechanism to heal mechanical damage. At the same time, the light-harvesting properties of the pure crystal useful in photocatalysis were preserved, but hydrogen production was enhanced since the hybrid nanostructures became more dispersible in water. Coarse-grained simulations suggest that these advantages are not specific to our chemical system and can be applicable to others in which there is a sufficiently strong interaction between the covalent polymers and small molecules.

METHODS

Materials Synthesis. Polymer **2** was synthesized by functionalizing poly(ethylene-*alt*-maleic anhydride) (PEAMA) with *N*-(5-aminopentyl)perylene-3,4-dicarboximide. Briefly, a solution of PEAMA, *N*-(5-aminopentyl)perylene-3,4-dicarboximide, and *N*,*N*-diisopropylethylamine (2 equiv with respect to the amine) was prepared in dimethylformamide at the ratio of the desired degree of polymer functionalization. The solution was stirred for 18 h at room temperature, and then the polymer was precipitated in 1 M HCl to yield a dark, red powder. The polymer was then immediately resuspended in a NaOH solution and heated to 80 °C for 18 h to hydrolyze any remaining anhydride moieties. The aqueous polymer solution was then dialyzed for 72 h against Milli-Q water using dialysis tubing with a molecular weight cutoff of 12−14 kDa. The final products were isolated by lyophilization to yield a bright red powder. CA **1**,[1] CA **3**,[42] and the thiomolybdate cluster catalyst[47] were prepared as reported previously in the literature. PEAMA with an average molecular weight M_w = 100,000−500,000 was purchased from Sigma-Aldrich and used as received. Detailed synthetic procedures are provided in the Supporting Information.

General Preparation of HBP Nanostructures. Aqueous solutions of polymer **2** (50 mM NaCl) and CA **1** (50 mM NaCl, 1 equiv NaOH) were mixed at different coassembly ratios (ϕ) by sonication and vortex mixing. Samples were annealed by heating them in a 95 °C water bath for 1 h and then slowly cooling the samples in a water bath to room temperature over 18 h.

TEM. For conventional dry-state TEM, samples were deposited on 300 mesh copper grids coated with a pure carbon film (Electron Microscopy Sciences) and stained with a 1 wt % uranyl acetate solution. Cryo-TEM samples were prepared using Vitrobot Mark IV (FEI) at room temperature with 95% humidity and 300 mesh lacey carbon grids (Electron Microscopy Sciences). Images were taken by a Gatan 831 CCD camera bottom mounted on a JEOL1230 microscope at 100 kV accelerating voltage. Detailed experimental procedures and supplemental data can be found in the Supporting Information.

X-ray Scattering. All experiments experiments were performed at Beamline 5-ID-D in the DuPont−Northwestern−Dow Collaborative Access team (DND-CAT) Synchrotron Research Center at the Advanced Photon Source, Argonne National Laboratory. X-ray energies of 17 keV for room-temperature measurements and 10 keV for variable-temperature (VT) measurements were selected using a double-crystal monochromator. For VT experiments, samples were heated at 1 °C per minute from 32 to 86 °C, held at 86 °C for 30 min, then cooled to 32 °C at 1 °C per minute taking in situ WAXS patterns every 10 min. Detailed experimental procedures and supplemental data are provided in the Supporting Information.

UV−vis Absorption Spectroscopy. Unless otherwise noted, room-temperature experiments were performed in a 0.05 mm path length, closed demountable quartz spectrophotometer cell (Starna Cells) using an Ocean Optics QEPro Spectrophotometer equipped with a DH-2000-Bal lamp and qpod 2e temperature control sample chamber.

Nanomechanical Measurements. AFM indentation and fracture tests were performed on a Veeco Dimension Icon scanning probe microscope (Veeco), Nanoscope V Controller (Bruker), at room temperature. The SNL-10 A probes (nominal tip radius 2 nm, Bruker) were used with ScanAsyst in air imaging mode (Peakforce Force Tapping) at 2 kHz with an amplitude of 150 nm. The samples were prepared by drop casting samples onto fresh mica substrates and then washing them with Milli-Q water. To obtain the force−separation curves, nano indentation was performed in "point and shoot" mode with ramp size/height of 50 nm and ramp velocity of 100 nm/s. Detailed experimental procedures and supplemental data are provided in the Supporting Information.

Rheological Measurements. Nanostructures were cross-linked by a carbodiimide-mediated coupling reaction using polyoxyethylene bis(amine) (MW = 3400) as the cross-linker. All rheological measurements were performed using an Anton Paar MCR302 rheometer with a P-PTD200 Peltier system for temperature control and a cone and plate fixture with 25 mm radius and 106 μm gap height. In a typical experiment, 150 μL of the gelled nanostructures was placed on the sample stage. The plunger was then lowered to the measuring position, and a humidity collar was added during the "sample trim" phase to prevent sample evaporation during the measurement. Frequency sweep experiments were performed at a strain amplitude of 0.1%, and the angular frequency was ramped down from 100 rad/s to 1 rad/s. Strain amplitude sweep experiments were performed at an angular frequency of 10 rad/s, and the strain amplitude was ramped up from 0.1% to 100%. Detailed synthetic procedures and supplemental data are provided in the Supporting Information.

Hydrogen Production Experiments. In a typical experiment, samples were prepared by adding 100 μL of HBP nanostructures (9.6 mM of PMI chromophore, 50 mM NaCl), 20 μL of the thiomolybdate cluster catalyst (180 μM), and 860 μL of ascorbic acid solution (1.7 M, pH 4) to a 9 mL screw cap vial with a silicone/PTFE septum. Vials were sealed and purged for 30 min with argon, then illuminated for 18 h using a home-built photoreactor made of white LEDs (Cree XLamp XT-E White LEDs 5000K). Analysis of gases evolved in the headspace during the photocatalysis was performed with a custom-built Shimadzu GC-2014 gas chromatography system equipped with a thermal conductivity detector. H_2 production was quantitatively detected using HayeSep T (1/16″, 7.5 m) and MS-5A (1/16″, 2.5 m) columns. Detailed experimental procedures and supplemental data are provided in the Supporting Information.

Coarse-Grained Simulation Methods. A detailed description of the coarse-grained representation of CA **1** and polymer **2** along with necessary force field parameters is provided in the Supporting Information. Briefly, the PMI chromophores are represented by 13 spheres connected into a rectangular rigid body 7.1 Å in length and 5.2 Å in width. Each sphere has a characteristic size of σ = 3.2 Å and interacts through a standard shifted-truncated Lennard-Jones (LJ) potential. The strong dipole moment of the PMI chromophores is represented by assigning a charge of $q = \pm 0.1q_0$, where q_0 is the unit electron charge, to the four corners of the coarse-grained PMI representation. The polymer backbone is modeled as a permanently (covalently) bonded bead−spring chain. Each bead is represented as a charged, shifted-truncated LJ sphere with size $\sigma_p = \sigma$ and charge $q = -q_0$, such that each monomer is represented by a bead. A fraction of beads (f) is chosen randomly and functionalized with a chromophore. We use f = 0.3 corresponding to a degree of functionalization of 30%.

The simulations were performed using the open-source MD package LAMMPS in the *NVT* ensemble. Typical runs contained 500

https://doi.org/10.1021/acsnano.2c00266
ACS Nano 2022, 16, 8993−9003

chromophore molecules in a 3D periodic cubic box with box length 200σ. The initial configuration was obtained by randomly positioning chromophore molecules in the box. We applied a Langevin thermostat with damping parameter 100τ and time unit $\tau = \sigma(m/k_BT)^{1/2}$ defined by the mass of the individual beads m. All simulations were conducted with a time step $\Delta t = 0.005\tau$. Equilibrium nanostructures were obtained by annealing the system for 4×10^8 timesteps with a linear temperature ramp from $T^* = 3$ to $T^* = 1$.

Initial configurations for simulations of shear and yielding were determined based on the eigenvectors of the radius of gyration tensor from the final, equilibrated structures obtained from the annealing simulations. The eigenvector with the largest eigenvalue (i.e., nanostructure length) was oriented with the x-axis, and the eigenvector with the second largest eigenvalue (i.e., nanostructure width) was oriented along the y-axis. The center of mass of the structure was placed at $x = 0$. Each end of the nanostructure was "clamped" together as a single rigid body and a force f_y was exerted on the center of mass of one end, to apply a shearing force to the nanostructures. The nonclamped parts of the nanostructure were simulated using the MD scheme described above, and force–extension curves were calculated based on the center of mass to which the force f_y was applied. Supplemental data is provided in the Supporting Information.

ASSOCIATED CONTENT

Supporting Information

The Supporting Information is available free of charge at https://pubs.acs.org/doi/10.1021/acsnano.2c00266.

Full descriptions of the synthetic methods, experimental procedures, CG-MD simulations, analytical theory, and supplemental data for X-ray scattering, UV–vis absorption spectroscopy, TEM, Cryo-TEM, AFM, and rheology experiments (PDF)

Video of the fracture behavior for hybrid nanostructures under shear (MP4)

AUTHOR INFORMATION

Corresponding Authors

Erik Luijten − *Department of Materials Science and Engineering, Department of Chemistry, Department of Physics and Astronomy, and Department of Engineering Sciences and Applied Mathematics, Northwestern University, Evanston, Illinois 60208, United States;* orcid.org/0000-0003-2364-1866; Email: luijten@northwestern.edu

Samuel I. Stupp − *Department of Materials Science and Engineering, Department of Chemistry, and Department of Biomedical Engineering, Northwestern University, Evanston, Illinois 60208, United States; Simpson Querrey Institute for BioNanotechnology and Department of Medicine, Northwestern University, Chicago, Illinois 60611, United States;* orcid.org/0000-0002-5491-7442; Email: s-stupp@northwestern.edu

Authors

Eric P. Bruckner − *Department of Materials Science and Engineering, Northwestern University, Evanston, Illinois 60208, United States;* orcid.org/0000-0002-9557-8029

Tine Curk − *Department of Materials Science and Engineering, Northwestern University, Evanston, Illinois 60208, United States;* orcid.org/0000-0002-2167-5336

Luka Đorđević − *Department of Chemistry, Northwestern University, Evanston, Illinois 60208, United States; Simpson Querrey Institute for BioNanotechnology, Northwestern University, Chicago, Illinois 60611, United States;* orcid.org/0000-0002-8346-7110

Ziwei Wang − *Department of Physics and Astronomy, Northwestern University, Evanston, Illinois 60208, United States;* orcid.org/0000-0002-2651-0813

Yang Yang − *Simpson Querrey Institute for BioNanotechnology, Northwestern University, Chicago, Illinois 60611, United States;* orcid.org/0000-0003-2409-5529

Ruomeng Qiu − *Department of Chemistry, Northwestern University, Evanston, Illinois 60208, United States;* orcid.org/0000-0001-7916-1509

Adam J. Dannenhoffer − *Department of Materials Science and Engineering, Northwestern University, Evanston, Illinois 60208, United States*

Hiroaki Sai − *Department of Materials Science and Engineering, Northwestern University, Evanston, Illinois 60208, United States; Simpson Querrey Institute for BioNanotechnology, Northwestern University, Chicago, Illinois 60611, United States;* orcid.org/0000-0002-4268-2148

Jacob Kupferberg − *Department of Materials Science and Engineering, Northwestern University, Evanston, Illinois 60208, United States;* orcid.org/0000-0002-7480-5755

Liam C. Palmer − *Department of Chemistry, Northwestern University, Evanston, Illinois 60208, United States; Simpson Querrey Institute for BioNanotechnology, Northwestern University, Chicago, Illinois 60611, United States;* orcid.org/0000-0003-0804-1168

Complete contact information is available at: https://pubs.acs.org/10.1021/acsnano.2c00266

Author Contributions

#E.P.B. and T.C. contributed equally. E.P.B., L.D., A.J.D., H.S., and S.I.S. designed the experiments. E.P.B., L.D., A.J.D., R.Q., Y.Y., J.K., and H.S. performed the experimental work. T.C., Z.W., and E.L. designed the theoretical model and performed the simulations. E.P.B., T.C, L.C.P, E.L., and S.I.S. wrote the paper.

Funding

The experimental work was supported by a grant from the National Science Foundation (NSF DMR-1508731). The theoretical model and simulations presented in this research were supported as part of the Center for Bio-Inspired Energy Science (CBES), an Energy Frontier Research Center funded by the U.S. Department of Energy (DOE), Office of Science, Basic Energy Sciences (BES), under award no. DE-SC0000989.

Notes

The authors declare no competing financial interest.

ACKNOWLEDGMENTS

E.P.B. gratefully acknowledges support by the Department of Defense, Army Research Office, through the National Defense Science and Engineering Graduate Fellowship, 32 CFR 168a. T.C. acknowledges support from the E.U. Horizon 2020 program through the Marie Skłodowska-Curie fellowship no. 845032. Z.W. gratefully acknowledges support from a Ryan Fellowship and the International Institute for Nanotechnology (IIN) at Northwestern University. This work made use of the IMSERC at Northwestern University for MS and NMR services, which has received support from the Soft and Hybrid Nanotechnology Experimental (SHyNE) Resource (NSF ECCS-1542205), the State of Illinois, and the IIN. Major

https://doi.org/10.1021/acsnano.2c00266
ACS Nano 2022, 16, 8993−9003

portions of this work were performed at the DuPont−Northwestern−Dow Collaborative Access Team (DND-CAT) located at Sector 5 of the Advanced Photon Source. DND-CAT is supported by Northwestern University, E.I. DuPont de Nemours & Co., and The Dow Chemical Company. This research used resources of the Advanced Photon Source, a U.S. DOE Office of Science User Facility operated by Argonne National Laboratory under contract no. DE-AC02-06CH11357. This work made use of the BioCryo facility of Northwestern University's NUANCE Center, which has received support from the SHyNE Resource (NSF ECCS-2025633), the IIN, and Northwestern's Materials Research Center (MRSEC) program (NSF DMR-1720139). This work also made use of the CryoCluster equipment, which has received support from the MRI program (NSF DMR-1229693), and of the MatCI Facility supported by the MRSEC program. The computational research was made possible in part through the computational resources provided by the Quest high performance computing facility at Northwestern University.

REFERENCES

(1) Weingarten, A. S.; Kazantsev, R. V.; Palmer, L. C.; McClendon, M.; Koltonow, A. R.; Samuel, A. P. S.; Kiebala, D. J.; Wasielewski, M. R.; Stupp, S. I. Self-Assembling Hydrogel Scaffolds for Photocatalytic Hydrogen Production. *Nat. Chem.* **2014**, *6* (11), 964−970.

(2) Noriega, R.; Rivnay, J.; Vandewal, K.; Koch, F. P. V.; Stingelin, N.; Smith, P.; Toney, M. F.; Salleo, A. A General Relationship between Disorder, Aggregation and Charge Transport in Conjugated Polymers. *Nat. Mater.* **2013**, *12* (11), 1038−1044.

(3) Tayi, A. S.; Shveyd, A. K.; Sue, A. C.-H.; Szarko, J. M.; Rolczynski, B. S.; Cao, D.; Kennedy, T. J.; Sarjeant, A. A.; Stern, C. L.; Paxton, W. F.; Wu, W.; Dey, S. K.; Fahrenbach, A. C.; Guest, J. R.; Mohseni, H.; Chen, L. X.; Wang, K. L.; Stoddart, J. F.; Stupp, S. I. Room-Temperature Ferroelectricity in Supramolecular Networks of Charge-Transfer Complexes. *Nature* **2012**, *488* (7412), 485−489.

(4) Miyajima, D.; Araoka, F.; Takezoe, H.; Kim, J.; Kato, K.; Takata, M.; Aida, T. Ferroelectric Columnar Liquid Crystal Featuring Confined Polar Groups Within Core−Shell Architecture. *Science* **2012**, *336* (6078), 209−213.

(5) Trigg, E. B.; Gaines, T. W.; Maréchal, M.; Moed, D. E.; Rannou, P.; Wagener, K. B.; Stevens, M. J.; Winey, K. I. Self-Assembled Highly Ordered Acid Layers in Precisely Sulfonated Polyethylene Produce Efficient Proton Transport. *Nat. Mater.* **2018**, *17* (8), 725−731.

(6) Yu, C.-J.; Krzyaniak, M. D.; Fataftah, M. S.; Wasielewski, M. R.; Freedman, D. E. A Concentrated Array of Copper Porphyrin Candidate Qubits. *Chem. Sci.* **2019**, *10* (6), 1702−1708.

(7) Buitrago, C. F.; Jenkins, J. E.; Opper, K. L.; Aitken, B. S.; Wagener, K. B.; Alam, T. M.; Winey, K. I. Room Temperature Morphologies of Precise Acid- and Ion-Containing Polyethylenes. *Macromolecules* **2013**, *46* (22), 9003−9012.

(8) Buitrago, C. F.; Alam, T. M.; Opper, K. L.; Aitken, B. S.; Wagener, K. B.; Winey, K. I. Morphological Trends in Precise Acid- and Ion-Containing Polyethylenes at Elevated Temperature. *Macromolecules* **2013**, *46* (22), 8995−9002.

(9) Middleton, L. R.; Szewczyk, S.; Azoulay, J.; Murtagh, D.; Rojas, G.; Wagener, K. B.; Cordaro, J.; Winey, K. I. Hierarchical Acrylic Acid Aggregate Morphologies Produce Strain-Hardening in Precise Polyethylene-Based Copolymers. *Macromolecules* **2015**, *48* (11), 3713−3724.

(10) Trigg, E. B.; Tiegs, B. J.; Coates, G. W.; Winey, K. I. High Morphological Order in a Nearly Precise Acid-Containing Polymer and Ionomer. *ACS Macro Lett.* **2017**, *6* (9), 947−951.

(11) Gaines, T. W.; Trigg, E. B.; Winey, K. I.; Wagener, K. B. High Melting Precision Sulfone Polyethylenes Synthesized by ADMET Chemistry. *Macromol. Chem. Phys.* **2016**, *217* (21), 2351−2359.

(12) Gaines, T. W.; Bell, M. H.; Trigg, E. B.; Winey, K. I.; Wagener, K. B. Precision Sulfonic Acid Polyolefins via Heterogenous to Homogenous Deprotection. *Macromol. Chem. Phys.* **2018**, *219* (11), 1700634.

(13) Yan, L.; Häußler, M.; Bauer, J.; Mecking, S.; Winey, K. I. Monodisperse and Telechelic Polyethylenes Form Extended Chain Crystals with Ionic Layers. *Macromolecules* **2019**, *52* (13), 4949−4956.

(14) Staiger, A.; Paren, B. A.; Zunker, R.; Hoang, S.; Häußler, M.; Winey, K. I.; Mecking, S. Anhydrous Proton Transport within Phosphonic Acid Layers in Monodisperse Telechelic Polyethylenes. *J. Am. Chem. Soc.* **2021**, *143* (40), 16725−16733.

(15) Hudson, Z. M.; Lunn, D. J.; Winnik, M. A.; Manners, I. Colour-Tunable Fluorescent Multiblock Micelles. *Nat. Commun.* **2014**, *5* (1), 3372.

(16) Qiu, H.; Gao, Y.; Boott, C. E.; Gould, O. E. C.; Harniman, R. L.; Miles, M. J.; Webb, S. E. D.; Winnik, M. A.; Manners, I. Uniform Patchy and Hollow Rectangular Platelet Micelles from Crystallizable Polymer Blends. *Science* **2016**, *352* (6286), 697−701.

(17) Merg, A. D.; van Genderen, E.; Bazrafshan, A.; Su, H.; Zuo, X.; Touponse, G.; Blum, T. B.; Salaita, K.; Abrahams, J. P.; Conticello, V. P. Seeded Heteroepitaxial Growth of Crystallizable Collagen Triple Helices: Engineering Multifunctional Two-Dimensional Core−Shell Nanostructures. *J. Am. Chem. Soc.* **2019**, *141* (51), 20107−20117.

(18) Jin, X.-H.; Price, M. B.; Finnegan, J. R.; Boott, C. E.; Richter, J. M.; Rao, A.; Menke, S. M.; Friend, R. H.; Whittell, G. R.; Manners, I. Long-Range Exciton Transport in Conjugated Polymer Nanofibers Prepared by Seeded Growth. *Science* **2018**, *360* (6391), 897−900.

(19) Tian, J.; Zhang, Y.; Du, L.; He, Y.; Jin, X.-H.; Pearce, S.; Eloi, J.-C.; Harniman, R. L.; Alibhai, D.; Ye, R.; Phillips, D. L.; Manners, I. Tailored Self-Assembled Photocatalytic Nanofibres for Visible-Light-Driven Hydrogen Production. *Nat. Chem.* **2020**, *12* (12), 1150−1156.

(20) Klinger, D.; Wang, C. X.; Connal, L. A.; Audus, D. J.; Jang, S. G.; Kraemer, S.; Killops, K. L.; Fredrickson, G. H.; Kramer, E. J.; Hawker, C. J. A Facile Synthesis of Dynamic, Shape-Changing Polymer Particles. *Angew. Chem., Int. Ed.* **2014**, *53* (27), 7018−7022.

(21) Tong, Z.; Zhang, R.; Ma, P.; Xu, H.; Chen, H.; Li, Y.; Yu, W.; Zhuo, W.; Jiang, G. Surfactant-Mediated Crystallization-Driven Self-Assembly of Crystalline/Ionic Complexed Block Copolymers in Aqueous Solution. *Langmuir* **2017**, *33* (1), 176−183.

(22) Feng, X.; Tousley, M. E.; Cowan, M. G.; Wiesenauer, B. R.; Nejati, S.; Choo, Y.; Noble, R. D.; Elimelech, M.; Gin, D. L.; Osuji, C. O. Scalable Fabrication of Polymer Membranes with Vertically Aligned 1 Nm Pores by Magnetic Field Directed Self-Assembly. *ACS Nano* **2014**, *8* (12), 11977−11986.

(23) Li, C.; Cho, J.; Yamada, K.; Hashizume, D.; Araoka, F.; Takezoe, H.; Aida, T.; Ishida, Y. Macroscopic Ordering of Helical Pores for Arraying Guest Molecules Noncentrosymmetrically. *Nat. Commun.* **2015**, *6* (1), 8418.

(24) Feng, X.; Kawabata, K.; Cowan, M. G.; Dwulet, G. E.; Toth, K.; Sixdenier, L.; Haji-Akbari, A.; Noble, R. D.; Elimelech, M.; Gin, D. L.; Osuji, C. O. Single Crystal Texture by Directed Molecular Self-Assembly along Dual Axes. *Nat. Mater.* **2019**, *18* (11), 1235−1243.

(25) Brannum, M. T.; Steele, A. M.; Venetos, M. C.; Korley, L. T. J.; Wnek, G. E.; White, T. J. Light Control with Liquid Crystalline Elastomers. *Adv. Opt. Mater.* **2019**, *7* (6), 1801683.

(26) Tabrizi, M.; Ware, T. H.; Shankar, M. R. Voxelated Molecular Patterning in Three-Dimensional Freeforms. *ACS Appl. Mater. Interfaces* **2019**, *11* (31), 28236−28245.

(27) Ware, T. H.; McConney, M. E.; Wie, J. J.; Tondiglia, V. P.; White, T. J. Voxelated Liquid Crystal Elastomers. *Science* **2015**, *347* (6225), 982−984.

(28) Kowalski, B. A.; Tondiglia, V. P.; Guin, T.; White, T. J. Voxel Resolution in the Directed Self-Assembly of Liquid Crystal Polymer Networks and Elastomers. *Soft Matter* **2017**, *13* (24), 4335−4340.

(29) Santos, P. J.; Gabrys, P. A.; Zornberg, L. Z.; Lee, M. S.; Macfarlane, R. J. Macroscopic Materials Assembled from Nanoparticle Superlattices. *Nature* **2021**, *591* (7851), 586−591.

https://doi.org/10.1021/acsnano.2c00266
ACS Nano 2022, 16, 8993−9003

(30) Amunts, A.; Drory, O.; Nelson, N. The Structure of a Plant Photosystem I Supercomplex at 3.4 Å Resolution. *Nature* **2007**, *447* (7140), 58−63.
(31) Umena, Y.; Kawakami, K.; Shen, J.-R.; Kamiya, N. Crystal Structure of Oxygen-Evolving Photosystem II at a Resolution of 1.9 Å. *Nature* **2011**, *473* (7345), 55−60.
(32) de Loos, M.; van Esch, J.; Stokroos, I.; Kellogg, R. M.; Feringa, B. L. Remarkable Stabilization of Self-Assembled Organogels by Polymerization. *J. Am. Chem. Soc.* **1997**, *119* (51), 12675−12676.
(33) Masuda, M.; Jonkheijm, P.; Sijbesma, R. P.; Meijer, E. W. Photoinitiated Polymerization of Columnar Stacks of Self-Assembled Trialkyl-1,3,5-Benzenetricarboxamide Derivatives. *J. Am. Chem. Soc.* **2003**, *125* (51), 15935−15940.
(34) Varela-Aramburu, S.; Su, L.; Mosquera, J.; Morgese, G.; Schoenmakers, S. M. C.; Cardinaels, R.; Palmans, A. R. A.; Meijer, E. W. Introducing Hyaluronic Acid into Supramolecular Polymers and Hydrogels. *Biomacromolecules* **2021**, *22* (11), 4633−4641.
(35) Ghosh, S.; Ramakrishnan, S. Small-Molecule-Induced Folding of a Synthetic Polymer. *Angew. Chem. Int. Ed* **2005**, *117* (34), 5577−5583.
(36) Jin, W.; Fukushima, T.; Kosaka, A.; Niki, M.; Ishii, N.; Aida, T. Controlled Self-Assembly Triggered by Olefin Metathesis: Cross-Linked Graphitic Nanotubes from an Amphiphilic Hexa-Peri-Hexabenzocoronene. *J. Am. Chem. Soc.* **2005**, *127* (23), 8284−8285.
(37) Stingelin-Stutzmann, N.; Smits, E.; Wondergem, H.; Tanase, C.; Blom, P.; Smith, P.; de Leeuw, D. Organic Thin-Film Electronics from Vitreous Solution-Processed Rubrene Hypereutectics. *Nat. Mater.* **2005**, *4* (8), 601−606.
(38) Chen, J.; Shao, M.; Xiao, K.; He, Z.; Li, D.; Lokitz, B. S.; Hensley, D. K.; Kilbey, S. M.; Anthony, J. E.; Keum, J. K.; Rondinone, A. J.; Lee, W.-Y.; Hong, S.; Bao, Z. Conjugated Polymer-Mediated Polymorphism of a High Performance, Small-Molecule Organic Semiconductor with Tuned Intermolecular Interactions, Enhanced Long-Range Order, and Charge Transport. *Chem. Mater.* **2013**, *25* (21), 4378−4386.
(39) Bronshtein, I.; Weissman, H.; Kaplan-Ashiri, I.; Rybtchinski, B. Crystallization of Small Organic Molecules in a Polymer Matrix: Multistep Mechanism Enables Structural Control. *Small* **2019**, *15* (38), 1902936.
(40) Dannenhoffer, A. J.; Sai, H.; Harutyunyan, B.; Narayanan, A.; Powers-Riggs, N. E.; Edelbrock, A. N.; Passarelli, J. V.; Weigand, S. J.; Wasielewski, M. R.; Bedzyk, M. J.; Palmer, L. C.; Stupp, S. I. Growth of Extra-Large Chromophore Supramolecular Polymers for Enhanced Hydrogen Production. *Nano Lett.* **2021**, *21* (9), 3745−3752.
(41) Weingarten, A. S.; Kazantsev, R. V.; Palmer, L. C.; Fairfield, D. J.; Koltonow, A. R.; Stupp, S. I. Supramolecular Packing Controls H_2 Photocatalysis in Chromophore Amphiphile Hydrogels. *J. Am. Chem. Soc.* **2015**, *137* (48), 15241−15246.
(42) Kazantsev, R. V.; Dannenhoffer, A. J.; Aytun, T.; Harutyunyan, B.; Fairfield, D. J.; Bedzyk, M. J.; Stupp, S. I. Molecular Control of Internal Crystallization and Photocatalytic Function in Supramolecular Nanostructures. *Chem.* **2018**, *4* (7), 1596−1608.
(43) Sai, H.; Lau, G. C.; Dannenhoffer, A. J.; Chin, S. M.; Đorđević, L.; Stupp, S. I. Imaging Supramolecular Morphogenesis with Confocal Laser Scanning Microscopy at Elevated Temperatures. *Nano Lett.* **2020**, *20* (6), 4234−4241.
(44) Stupp, S. I.; Clemons, T. D.; Carrow, J. K.; Sai, H.; Palmer, L. C. Supramolecular and Hybrid Bonding Polymers. *Isr. J. Chem.* **2020**, *60*, 124−131.
(45) Shimizu, T. The Dilute Solution Properties of Maleic Anhydride and Maleic Acid Copolymers. II-Unperturbed Dimensions and Persistence Lengths of Chains in Solution. *Polymer* **1981**, *22* (2), 231−234.
(46) Hestand, N. J.; Kazantsev, R. V.; Weingarten, A. S.; Palmer, L. C.; Stupp, S. I.; Spano, F. C. Extended-Charge-Transfer Excitons in Crystalline Supramolecular Photocatalytic Scaffolds. *J. Am. Chem. Soc.* **2016**, *138* (36), 11762−11774.
(47) Kibsgaard, J.; Jaramillo, T. F.; Besenbacher, F. Building an Appropriate Active-Site Motif into a Hydrogen-Evolution Catalyst with Thiomolybdate $[Mo_3S_{13}]^{2-}$ Clusters. *Nat. Chem.* **2014**, *6* (3), 248−253.

https://doi.org/10.1021/acsnano.2c00266
ACS Nano 2022, 16, 8993−9003